

Imaging material functionality through three-dimensional nanoscale tracking of energy flow

Milan Delor^{1,2,7}, Hannah L. Weaver^{1,2,3}, QinQin Yu³ and Naomi S. Ginsberg^{1,2,3,4,5,6*}

The ability of energy carriers to move between atoms and molecules underlies biochemical and material function. Understanding and controlling energy flow, however, requires observing it on ultrasmall and ultrafast spatio-temporal scales, where energetic and structural roadblocks dictate the fate of energy carriers. Here, we developed a non-invasive optical scheme that leverages non-resonant interferometric scattering to track tiny changes in material polarizability created by energy carriers. We thus map evolving energy carrier distributions in four dimensions of spacetime with few-nanometre lateral precision and directly correlate them with material morphology. We visualize exciton, charge and heat transport in polyacene, silicon and perovskite semiconductors and elucidate how disorder affects energy flow in three dimensions. For example, we show that morphological boundaries in polycrystalline metal halide perovskites possess lateral- and depth-dependent resistivities, blocking lateral transport for surface but not bulk carriers. We also reveal strategies for interpreting energy transport in disordered environments that will direct the design of defect-tolerant materials for the semiconductor industry of tomorrow.

Energy flow is central to all biological, chemical and material functionality. Elucidating how distinct macroscopic functions emerge from different structural arrangements of atoms and molecules requires an understanding of how energy is transduced and transported between a system's building blocks. Materials science is undergoing a revolution with a burst of new high-performance semiconductors made from a diversity of readily tunable molecular building blocks^{1–3}. Nevertheless, a fundamental understanding of why some semiconductors outperform others remains elusive⁴, inhibiting rational materials design. The difficulty in gaining such predictive power is compounded by nanoscale spatio-energetic disorder, manifested in defects, impurities and interfaces, that gives rise to spatio-temporally heterogeneous energy transport. Elucidating how the microscopic details of a material relate to its emergent optoelectronic properties will therefore require the ability to individually and systematically correlate nanoscale structure with energy flow across a wide range of systems.

Resolving how energy flow is affected by spatio-energetic disorder requires tracking energy carriers over a wide spatio-temporal range—nanometres to micrometres and picoseconds to milliseconds—and directly correlating the measurements with material morphology. This correlation notwithstanding, powerful spatio-temporally resolved approaches have recently been developed to visualize nanoscale energy flow using photoluminescence^{5–7}, transient absorption^{8–11} or electron scattering¹² as contrast mechanisms. They achieve femtosecond time resolution^{10,12}, large dynamic range⁵, chemical specificity^{5–7,10} and excellent spatial sensitivity^{5–7}. Nevertheless, their current implementations mostly track only a subset of energy carrier types and rely on samples that have specific optical or electronic properties, such as being absorbing yet having low optical density¹⁰, having large Stokes shifts⁶ and appreciable emission^{5,7} or being resistant to electron beams¹². They also measure energy flow in only two dimensions, and most acquire a single

image pixel at a time. These constraints limit the breadth of samples and fundamental processes that can be studied. Overcoming these challenges, we developed an approach that leverages elastic scattering, a universal optical interaction, to track evolving distributions of any type of energy carrier in three spatial dimensions, irrespective of their optical properties, as they move through any material on picosecond to millisecond timescales. This approach enables simultaneous imaging of the nano- to microscale morphological features that define the spatio-energetic landscape of the material, providing the much-sought-after in situ structure–function correlations.

In our approach, we first introduce a diffraction-limited, short pump light pulse to generate a localized collection of energetic carriers. These carriers act as point scatterers in the sample by modifying local material electric polarizability. We subsequently probe the pump-induced changes to the scattering profile of the material at controllable time delays over a large sample area through which energy carriers diffuse (Fig. 1a and Supplementary Sections 1 and 2), thus imaging the evolving carrier distribution in space. Although related to transient absorption microscopy, our approach has two key advances that help it overcome the limitations of previous methods: it operates in a reflection geometry, and it images large areas using a wide-field probe. Beyond providing advantages related to sample generalizability and contrast (Supplementary Section 2.2), a reflection geometry enables the tracking of energy carriers in three dimensions (3D) by interfering a reflected reference field (for example, from the sample–substrate interface) with the back-scattered field arising from the probe interaction with the energy carriers and their immediate surroundings. The resulting interferometric image converts phase delays (due to the varying depth of the scatterer distribution compared with the well-defined interface) into amplitude contrast, providing a semi-quantitative depth profile of the carrier distribution. A large probe area considerably reduces acquisition time by acquiring a snapshot of the sample's scattering

¹Department of Chemistry, University of California Berkeley, Berkeley, CA, USA. ²STROBE, National Science Foundation Science and Technology Center, University of California Berkeley, Berkeley, CA, USA. ³Department of Physics, University of California Berkeley, Berkeley, CA, USA. ⁴Kavli Energy NanoSciences Institute, Berkeley, CA, USA. ⁵Material Sciences Division, Lawrence Berkeley National Laboratory, Berkeley, CA, USA. ⁶Molecular Biophysics and Integrated Bioimaging Division, Lawrence Berkeley National Laboratory, Berkeley, CA, USA. ⁷Present address: Department of Chemistry, Columbia University, New York, NY, USA. *e-mail: nsginsberg@berkeley.edu

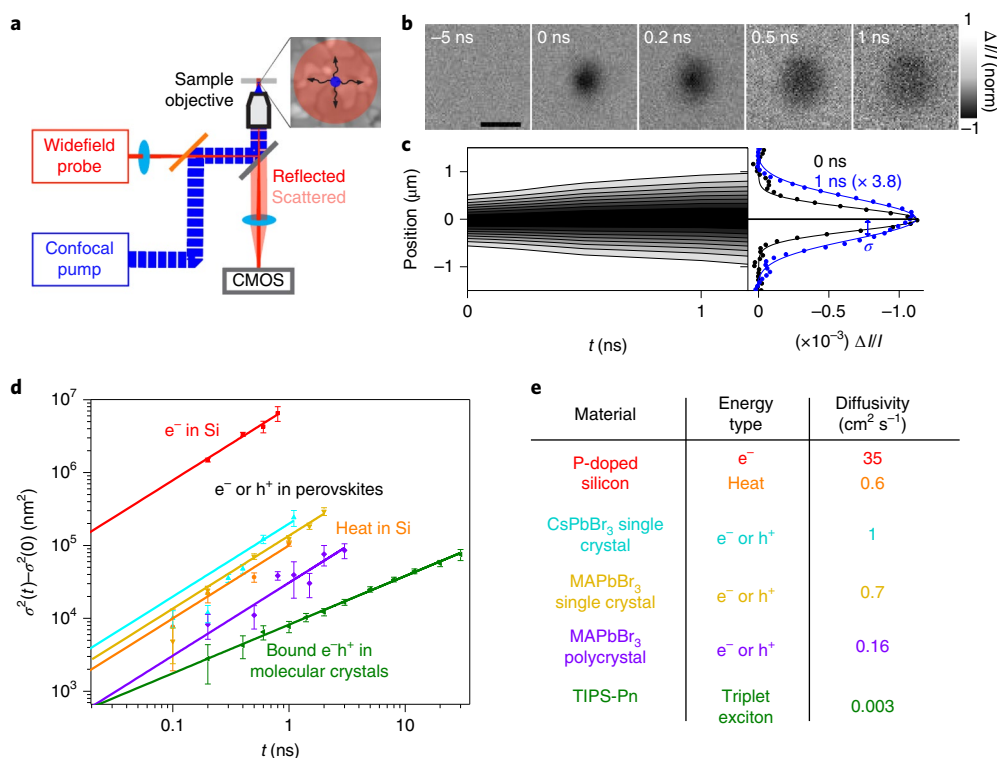


Fig. 1 | Visualizing semiconductor exciton, charge and heat transport across four orders of magnitude in space and time. **a**, StrobeSCAT set-up. A confocal pump (306 nm diameter, wavelength $\lambda = 440$ nm) and wide-field probe (8 μm diameter, $\lambda = 635$ nm) are overlapped in the sample. Probe light that is both scattered by the sample and reflected at the sample–substrate interface is imaged on the charged metal–oxide semiconductor (CMOS) camera. Full details are given in Supplementary Sections 1–6. **b**, Example stroboSCAT dataset for a MAPbBr₃ single crystal, showing charge carriers diffusing as a function of pump–probe time delay. The peak pump-injected carrier density is $2 \times 10^{18} \text{ cm}^{-3}$, and the probe is spectrally far from the band edge (570 nm). The peak power densities at the sample are on the order of 0.2 MW cm^{-2} , far below the onset of nonlinear optical effects. All stroboSCAT plots are generated by taking the difference between pump_{ON} and pump_{OFF} raw pixel intensities (I), normalized to the raw pump_{OFF} intensities, yielding $\Delta I/I$ contrast images. Scale bars, 1 μm . **c**, The spatio-temporal population distribution along the horizontal spatial axis is plotted, along with 1D Gaussian profiles extracted at 0 and 1 ns pump–probe delay. **d**, Charge, exciton or heat distributions versus time measured for a range of semiconductors (Supplementary Section 7). See panel **e** for colour coding. Error bars represent the 95% confidence intervals from Gaussian fits. All experiments are performed in a linear excitation regime, as confirmed by a lack of power dependence to extracted diffusivities. **e**, Diffusivities extracted from linear fits of the data in **d**.

profile in a single image exposure, obviating the need for sample, beam or detector scanning and providing morphological correlation with diffraction-limited resolution. The signal can also be spectrally resolved in the same instrument (Supplementary Section 1), a technique known as spectral interferometry^{13–15}. This technique does not track carrier motion through space but instead provides information on the sample’s spectral response to photoexcitation in localized regions of its heterogeneous landscape—a powerful tool when combined with the imaging mode of the instrument.

Inspired by advances in scattering-based interferometric and photothermal microscopies^{16–23} that achieve extremely sensitive detection of tiny scatterers down to single molecules, we call our approach stroboscopic scattering microscopy (strobeSCAT). Whereas interferometric scattering microscopy (iSCAT) allows single-particle tracking of nanoparticles and biomolecules, stroboSCAT opens a new range of possibilities for tracking the spatio-temporal evolution of distributions of photogenerated energy carriers. We use iSCAT’s formalism to treat the pump-induced contrast changes (Supplementary Section 2); a similar formalism based on the optical theorem has been used for transient spectral interferometry of quantum dots^{13,14}. Microscopically, both absorption and reflection originate from scattering. Macroscopically, however, most semiconductors possess refractive indices in the visible range that are dominated by their relatively wavelength-independent real

part (n) rather than by their imaginary part (k , which is responsible for absorption). For these high n/k ratios, stroboSCAT is primarily sensitive to changes in n (refs. ^{24–26}, Supplementary Section 2.2). Overall, stroboSCAT is a high-throughput method (<10 min acquisition for full spatio-temporally resolved datasets) to track time-evolving carrier distributions in 3D with high spatio-temporal resolution and in situ morphological correlation in a wide range of materials (for example, opaque or transparent, emissive or not emissive, composite or uniform). We show that these distinctive attributes enable detailed and model-free structure–function correlations in a broad range of materials, precisely pinpointing the origin of functional heterogeneity in disordered semiconductors.

We use stroboSCAT to visualize energy flow in a wide range of semiconductors, demonstrating its capability over four orders of magnitude in space and time, on both neutral and charged excitations migrating through organic, organic–inorganic and inorganic semiconductors. Before focusing on disordered semiconductors, we illustrate stroboSCAT imaging of carrier diffusion in an ordered semiconductor: Fig. 1b,c displays the spatial profile of charge carriers as a function of pump–probe delay in a methylammonium lead bromide (MAPbBr₃) perovskite single crystal. At 635 nm, the probe is spectrally far from the band edge (570 nm), primarily detecting changes in n . Using ultra-stable picosecond pulsed laser diodes, we achieve shot-noise-limited differential contrast with sensitivities

approaching 10^{-5} and a signal-to-noise ratio averaging 40 for up to a 1 ns pump–probe time delay with less than 1 min integration per time delay. In this simple example, the diffusivity D for the charge carriers can be modelled from the Gaussian distribution variance σ^2 of the scattering profile with time t : $2Dt = \sigma^2(t) - \sigma^2(0)$ (Supplementary Section 3). The achievable sample-dependent spatial precision, $\Delta\sigma(t) = \pm 2-10$ nm for a <1 min measurement per time delay (or $\Delta\sqrt{2Dt} = \pm 4-20$ nm), is not limited by diffraction but rather by fitting precision, which depends on signal-to-noise ratio^{5,10}. Figure 1d,e summarizes similar analyses on a variety of semiconductors using the same experimental set-up to image heat, neutral bound pairs of charges (excitons) and free charge carrier diffusion. As each type of energy carrier changes the local polarizability differently, the magnitude and sign of the stroboSCAT contrast differentiates coexisting types of energy carriers. For example, heat can generate opposite contrast to that of free charges, as we see in silicon (Supplementary Fig. 4).

Our results closely match published values for materials whose energy diffusivities have previously been determined^{27–30}, confirming stroboSCAT's viability. One notable observation in Fig. 1d,e is that carrier diffusivities in MAPbBr₃ are reduced more than fourfold in disordered polycrystalline films compared with those in single crystals. Nevertheless, the impact of domain interfaces on energy flow can be non-trivial, depending greatly on their type, size, distribution and composition. We use stroboSCAT to track and morphologically correlate energy flow up to, within and across energetic obstacles, using two classes of emerging semiconductors as case studies. Our results and corroborating simulations reveal that carrier trajectories are governed by highly anisotropic paths of least resistance, precluding the viability of diffusive models extracted from bulk or averaged measurements and calling for new ways to interpret and quantify energy flow in disordered environments.

We first explore the effect of low-curvature domain interfaces on exciton migration in polycrystalline 6,13-bis(triisopropylsilylethynyl)pentacene (TIPS-Pn)³¹ films. TIPS-Pn is a promising singlet-fission sensitizer for hybrid solar panels and represents an archetypal system in which to study energy transport in π -stacked molecular crystals (Fig. 2a)^{32,33}. In Fig. 2b, iSCAT images at two different probe field polarizations display two orthogonally oriented crystalline domains (light versus dark) separated by straight interfaces. Exciton migration imaged by stroboSCAT within a domain (Fig. 2c–e) shows that at early time delays, the migration is nonlinear, lending support to previous reports that attribute this behaviour to the interchange between fast-diffusing singlet and slow-diffusing triplet pair excitations³⁴. Beyond 5 ns, the linear diffusion that we observe at $D = 0.003$ cm² s⁻¹ (Supplementary Fig. 12) is consistent with the common interpretation of free triplet migration^{5,34}.

The key finding enabled by stroboSCAT is the degree to which individual grain boundaries hinder exciton transport in molecular crystals and that the extent of this hindrance varies widely. The narrow wedge-shaped central domain in this example provides an opportunity to systematically quantify the effect of domain confinement by interfaces on exciton migration (Fig. 2d). Population distribution expansion along the fast migration axis at red, orange and yellow spots highlighted in Fig. 2b,d are plotted in Fig. 2e. Comparing the bulk crystalline domain (red) and the most confined spot (yellow), we find that interfaces severely hinder exciton transport, slowing it approximately fourfold. Transport at the partially confined area (orange) can be accurately modelled piecewise, with free migration up to 3 ns (overlapping orange and red curves) and confined migration thereafter (where the orange curve parallels the yellow curve), indicating a transition from bulk-like to slower transport at an interface. We measured exciton migration in 15 different domains and at 17 different grain boundaries and found that (1) exciton transport is always slower at grain boundaries than in domains (Fig. 2f inset) and (2) transport speed is consistent in all

measured domains, whereas transport at grain boundaries is highly variable, as indicated by the normalized distribution of initial ($t = 0$) diffusivities in Fig. 2f. Indeed, interface formation kinetics, degree of lattice misorientations, and void and impurity concentrations will give rise to a wide range of transport behaviour at different interfaces. Thus, high-throughput and correlative measurements of exciton migration over nanometre length scales provide the crucial ability to investigate energy transport properties in situ for individual interfaces and surrounding crystal domains and to correlate these with their specific morphologies.

Although large crystalline domains separated by abrupt interfaces provide a systematic environment for testing the effects of crystalline mismatch on energy transport, a more commonly encountered morphology in polycrystalline semiconductors consists of sub- to few-micrometre-sized domains. In these materials, energy carriers almost inevitably encounter domain boundaries during their lifetimes. Grain boundaries and, more generally, morphological boundaries (MBs) between domains (which are most typically crystal grains) thus significantly impact bulk-averaged measures of energy flow such as charge mobility and recombination^{35,36}. There is, however, little consensus on the effect of MBs on the functional properties of a wide range of semiconductors. Nowhere is the debate currently more salient than with metal halide perovskites^{37–45}. For example, despite numerous studies suggesting that MBs in perovskites have large trap densities, act as recombination centres and impede carrier transport, photovoltaic efficiencies for polycrystalline films exceed 20% and do not necessarily scale favourably with grain size⁴⁶. The primary difficulty in resolving these paradoxes lies in elucidating how the functional impacts of MBs locally deviate from bulk-averaged metrics. This challenge is exacerbated by the vast diversity of preparation protocols for polycrystalline metal halide perovskites, which lead to radically different material properties⁴⁷. We show that visualizing carrier distributions in 3D as they trace the paths of least resistance through different halide perovskite films provides systematic and individualized detail on the effect of traps, the lateral- and depth-dependent conductive properties of MBs and the resulting spatio-temporal anisotropy of charge transport as a function of material morphology.

The stroboSCAT time series in Fig. 3a illustrates differences in charge carrier transport for three polycrystalline methylammonium lead iodide (MAPbI₃) films prepared using common protocols that lead to different domain sizes (Supplementary Section 4). As these samples are emissive, we also display the correlated steady-state wide-field emission pattern arising from carrier recombination⁴⁰ in Fig. 3b (Supplementary Section 1). The close correspondence between wide-field emission and stroboSCAT images at late time delays confirms that the full extent of carrier migration is captured by stroboSCAT. On average, films with smaller domains exhibit slower lateral carrier transport, confirming that MBs negatively affect interdomain carrier transport. From the data in Fig. 3a we extract lateral diffusion lengths (by azimuthally averaging and time-averaging over the first 2 ns) of 180 nm, 200 nm and 700 nm for films made respectively with PbAC₂, PbI₂ and PbCl₂ precursors.

In the largest-domain sample in Fig. 3a, the sign of the stroboSCAT contrast can reverse from negative to positive. By correlating stroboSCAT measurements with structural maps in the same field of view (Supplementary Section 8), we show that these contrast flips occur only at MBs. We rule out the possibility that the contrast flips arise from a change in carrier density, scattering amplitude or heat, as we do not observe these sign flips in any other region when varying the pump fluence over four orders of magnitude. We therefore attribute these contrast flips to a change in the phase of the interferometric cross-term combining the reflected and scattered fields (Supplementary Section 2). The cross-term phase depends linearly on the depth of the scattering objects with respect to the sample–substrate interface, providing a measure of the distribution

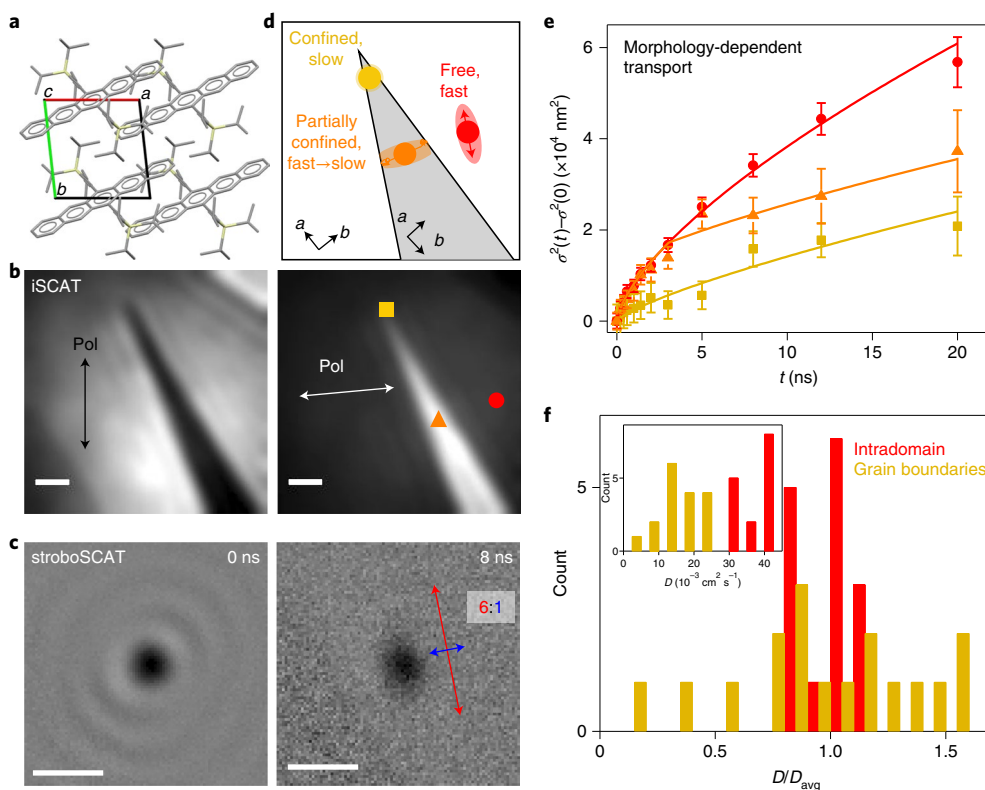


Fig. 2 | Morphology-dependent exciton transport in TIPS-Pn. **a**, Crystal structure of TIPS-Pn (ref. ³¹), displaying the orientation of the crystallographic *a* and *b* axes. Carbon atoms are grey, silicon atoms are yellow. **b**, iSCAT images at different polarizations (pol) showing two orthogonally oriented crystal domains. These images are bandpass-filtered to remove diffraction fringes near interfaces (Supplementary Fig. 8). Mean squared displacement curves measured at the positions depicted by the red circle, orange triangle and yellow square are displayed in panel **e**. **c**, Stroboscoped images at 0 and 8 ns delay in a crystalline domain (red spot in **b**), displaying anisotropic diffusion with sixfold faster transport along the π -stacked (red) axis of the crystal (Supplementary Fig. 9). The lab frame anisotropy directionality changes in different domains in relation to their crystal orientations. Both the pump (440 nm) and probe (640 nm) are resonant with ground-state absorption in this example. **d**, Schematic of exciton diffusion behaviour at three different spots: intradomain (red), confined (yellow) and intermediate transport scenarios (orange). **e**, Corresponding population expansion dynamics along the fast-diffusion axes. The pump is circularly polarized and the probe polarization is chosen to avoid contrast bias across domains (Supplementary Figs. 10 and 11). Error bars represent the 95% confidence intervals from Gaussian fits. **f**, Spot-to-spot variability of initial diffusivity D_0 , determined from the fitting function $f(t) = 2D_0t^\alpha$ where α is a free parameter, for intradomain and grain boundary-confined scenarios. Peak fluence is $140 \mu\text{J cm}^{-2}$ (Supplementary Fig. 12). Scale bars are all $1 \mu\text{m}$.

of scatterers along the optical axis^{48,49}. The resulting stroboscoped contrast is strongly negative for carriers located within ~ 30 nm of the interface and weakly positive for carriers located at depths of $\sim 50 \pm 20$ nm (Supplementary Fig. 21c). Thus, the localized regions of positive contrast in these films indicate that, at MBs, the density of carriers at depths around 50 nm is significantly larger than the density within 30 nm of the surface. This observation suggests that when a carrier encounters a MB near the surface of the film, the path of least resistance leads deeper into the film rather than across the feature, resulting in a very low density of surface carriers at MBs. In contrast, subsurface carriers appear to cross MBs almost unimpeded. Our findings provide important mechanistic insight as to why conductive atomic force microscopy on MAPbI₃ films indicates infinite MB resistance at the film surface but carriers still somehow migrate to adjacent domains⁴³.

We corroborate our interpretation of the contrast flips using spectral interferometry (Supplementary Section 1): using near-diffraction-limited pump and probe beams, we measure the pump-induced spectral changes around the band edge of MAPbI₃. Figure 3c shows representative spectral response profiles within a domain (black trace) versus at a boundary (grey trace) at $t=0$ for the large-domain MAPbI₃ film. The dispersive line shape within the domain corresponds closely to that reported in the literature from bulk

transient reflectance spectroscopy of MAPbI₃ single crystals²⁵. In contrast, the response from MBs occurs at the same spectral position but is inverted, indicating a $\sim \pi$ phase shift of the signal at the MB relative to within the domain. The conserved spectral position shows that the primary difference between the intradomain and MB response is the phase, not the presence of another excited state species or the chemical composition at the MB. Additional datasets (Supplementary Figs. 19 and 20) show that intradomain signals always show the same dispersive line shape, and that phase shifts between $\pi/2$ and π always occur at MBs. This trend, which persists across ~ 50 measured regions, confirms that charge carriers cross MBs only below the film surface in our samples.

We characterize depth-dependent MB resistivities by time-propagating finite element simulations of carrier diffusion in heterogeneous MAPbI₃ films with a simple model (details provided in Supplementary Section 9). We simulate the carrier distribution evolution in a 2D x - z film slice following an initial localized excitation (Fig. 3d). To obtain reasonable agreement with experiments, the MBs must be parametrized by resistivities that are infinite at the film surface, concurring with results from atomic force microscopy experiments⁴³, but that rapidly drop as a function of depth, approaching nearly intradomain resistivity within ~ 50 nm of the film surface. Figure 3e displays the resulting carrier distribution

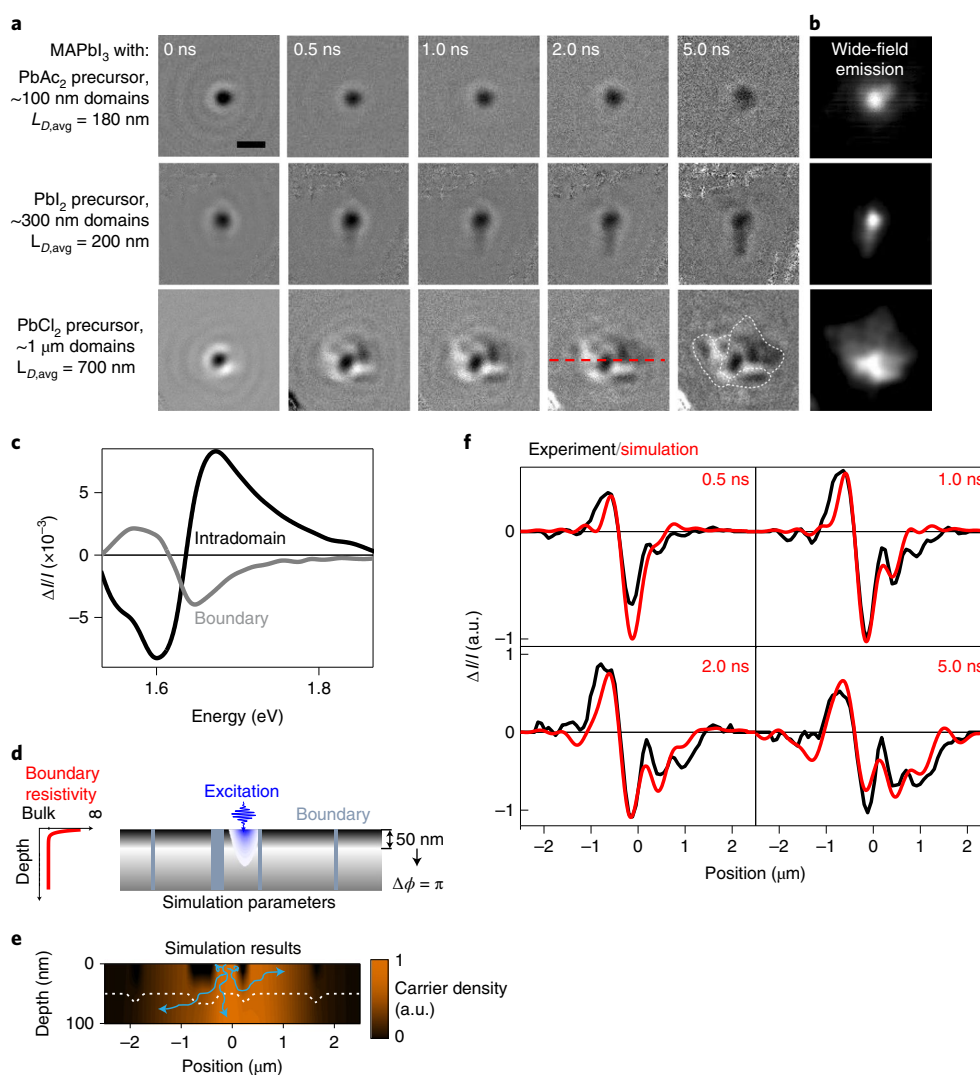


Fig. 3 | Heterogeneous charge carrier transport in polycrystalline MAPbI₃. **a**, StrobeSCAT time series on three MAPbI₃ samples prepared from different precursors. **b**, Corresponding wide-field emission images from confocal excitation. Domain sizes are measured using atomic force microscopy (Supplementary Fig. 13). 2D diffusion lengths $L_{D,avg} = \sqrt{4D\tau}$ are azimuthally averaged and are calculated over a truncated lifetime of $\tau = 2$ ns only, during which D is approximately constant. Normalized stroboSCAT contrast is represented in greyscale with black (white) representing the most negative (positive) value. The MB positions for the large-domain film are depicted using dashed white lines. The signals do not depend on pump or probe polarization. The scale bar is 1 μm and applies to all panels in **a**. Peak carrier density is $1.5 \times 10^{18} \text{ cm}^{-3}$. The probe at 640 nm is above the bandgap of MAPbI₃ but away from the band edge (760 nm) where the largest photoinduced absorption change occurs. **c**, Spectrally resolved interferometric signal near the MAPbI₃ band edge using the same excitation conditions but probing using broadband white light, showing a phase-flipped signal at MBs compared with the signal within domains. **d**, A sketch of a film cross-section used in simulations in which MB positions were derived by comparing the simulations in **f** to the phase-sensitive stroboSCAT images for the PbCl₂ precursor film in **a**. Greyscale shading represents the depth-dependent contrast expected from stroboSCAT measurements in MAPbI₃, resulting from an interferometric phase change of $\Delta\Phi = \pi$ for scatterers located at a depth of 50 nm (Supplementary Fig. 21c). **e**, Results of simulations using time-propagated finite element analysis of carrier migration along the line cut indicated by the horizontal red line in **a**, displaying the carrier distribution (orange shading) in the top 100 nm of the film 5 ns after excitation. The dashed white trace is the average axial position of the carrier distribution. Calculated distributions for other time delays are shown in Supplementary Fig. 22. The light-blue traces are hypothetical carrier trajectories that are consistent with the observed carrier distributions. **f**, Quantitative agreement of experimental stroboSCAT data with simulation results after the simulation results have undergone appropriate contrast scaling and convolution with the apparatus' point-spread function. The MB positions and resistivities used in the simulation to fit the experimental data are shown in **d**. Further details and datasets are provided in Supplementary Figs. 14–24.

after 5 ns. The dashed white trace represents the average axial position of the carrier distribution, indicating how the carrier density peaks further beneath the surface at the MBs. To directly compare the simulation with experiment and constrain our model, the simulated carrier distributions are contrast-scaled according to Supplementary Fig. 21c and convolved with the point spread function of the instrument. Figure 3f plots the resulting traces for four

time delays, showing excellent agreement for these data and for additional structurally correlated datasets shown in Supplementary Section 9. The combination of experiments and simulations thus enables a semi-quantitative description of the 3D evolution of carrier distributions in these films: MBs act as impassable walls at the film surface, removing a lateral transport pathway for surface carriers. Carriers at depths below ~ 50 nm, however, cross almost

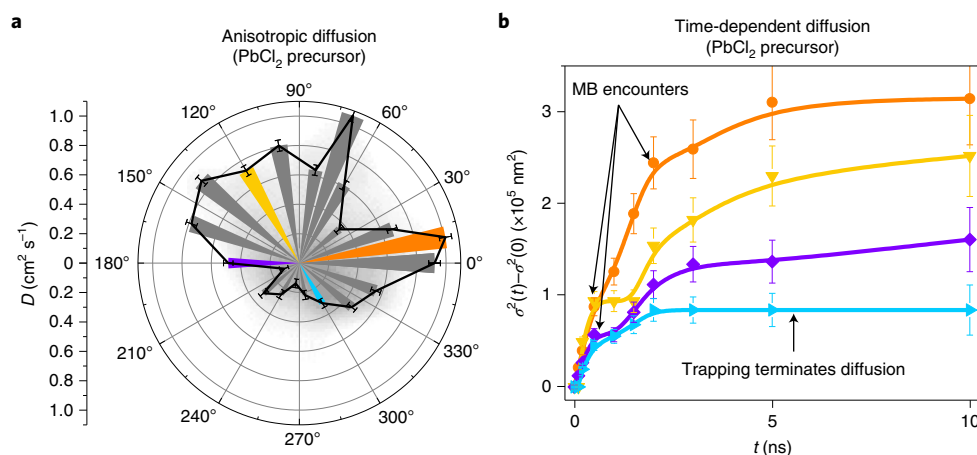


Fig. 4 | Quantifying spatial and temporal carrier transport heterogeneity in polycrystalline MAPbI₃. **a**, Angle-dependent diffusivities averaged over the first 2 ns for the PbCl₂ precursor data shown in Fig. 3a. **b**, Time-dependent diffusion for four representative azimuthal angles colour-coded in panel **a**. Error bars represent the standard deviation of the fits to several experimental datasets taken at the same location in the films. Curves represent a spline interpolation of the data points. Further analyses for films prepared from different precursors are presented in Supplementary Fig. 18.

unhindered into neighbouring domains. Within domains, unimpeded 3D migration quickly leads to uniform carrier distributions. Since stroboSCAT is most sensitive to carriers located near the surface (Supplementary Fig. 21c), where the contrast is negative, we clearly distinguish domains (negative contrast) from MBs (positive contrast). This unique axial sensitivity afforded by phase contrast therefore provides a comprehensive 3D picture of both the morphological and functional properties of these materials. Furthermore, by measuring multiple regions and different films, we reveal that each MB has its own conductivity profile, leading to interdomain energy carrier flow patterns that are highly anisotropic both axially and laterally (Supplementary Figs. 15 and 16).

To generalize our findings, we systematically quantify the degree of functional heterogeneity in these samples with further analyses. Figure 4a plots the initial angle-resolved charge carrier lateral diffusivity for MAPbI₃ prepared with the PbCl₂ precursor, which ranges from 0.1 cm² s⁻¹ to 1.1 cm² s⁻¹. The time dependence of lateral carrier motion along each of the four colour-coded directions in Fig. 4a is depicted in Fig. 4b. Although intradomain transport both before and after passing through a MB can be as high as 1.3 cm² s⁻¹, the terraces between the higher-slope portions of the curves observed in the time dependence in Fig. 4b illustrate how MB encounters seem to temporarily halt lateral energy flow. The final plateau in population expansion occurs within several nanoseconds, indicating that a large fraction of carriers stop migrating on timescales much shorter than the average carrier recombination time (379 ns, Supplementary Fig. 14). This termination indicates that at these fluences the carrier density decreases on a few-nanosecond timescale to below the material's trap-state density. Furthermore, it suggests that some traps do not act as recombination centres but may instead be hole- and/or electron-selective. This analysis emphasizes the importance of tracking carriers until diffusion terminates rather than extrapolating from the early-time constant diffusion through to the carrier lifetimes, which would falsely imply an average diffusion length in this sample of ~10 μm instead of ~1 μm. In summary, we show that moving beyond averaged metrics in all spatio-temporal dimensions is essential to answering multiple prominent questions surrounding these materials and to addressing the functional impacts of structural and electronic disorder. For example, we find that in our large-domain MAPbI₃ films, MBs (in many cases, grain boundaries) do not act as recombination centres and only substantially affect lateral transport for surface carriers, not bulk carriers. For charge extraction in planar photovoltaic architectures,

surface carriers are axially extracted and should therefore be minimally affected by MBs that are oriented perpendicular to the charge extraction layers.

Establishing the fundamental relationship between microscopic structural motifs and macroscopic function has been a long-standing multiscale challenge. In response, we devised a highly accessible and high-throughput strategy for measuring energy flow in situ that is universally applicable to different energy forms and material properties. Benefitting from the high spatio-temporal resolution, sensitivity and dynamic range of stroboSCAT, we demonstrated 3D measurement of energy flow through heterogeneous environments on pertinent scales, enabling direct correlation of the structure and functional connectivity in a broad range of semiconductors. We envision that stroboSCAT will impact the study of energy materials well beyond the scope of this present work and will eventually reach the ultimate sensitivity limit of tracking single energy carriers³⁰, permitting nanometric functional mapping using single-particle localization with few-nanometre precision in all spatial dimensions. Finally, using scattering as a contrast mechanism enables a comprehensive range of processes—not only energy flow but also the transport of chemical species or ions—to be studied with the same level of detail and could shed light on catalytic cycles and chemical energy storage.

Online content

Any methods, additional references, Nature Research reporting summaries, source data, statements of code and data availability and associated accession codes are available at <https://doi.org/10.1038/s41563-019-0498-x>.

Received: 2 November 2018; Accepted: 2 September 2019;

Published online: 07 October 2019

References

- García de Arquer, F. P., Armin, A., Meredith, P. & Sargent, E. H. Solution-processed semiconductors for next-generation photodetectors. *Nat. Rev. Mater.* **2**, 16100 (2017).
- Sirringhaus, H., Tessler, N. & Friend, R. Integrated optoelectronic devices based on conjugated polymers. *Science* **280**, 1741–1744 (1998).
- Scholes, G. D. & Rumbles, G. Excitons in nanoscale systems. *Nat. Mater.* **5**, 683–696 (2006).
- Brenner, T. M. et al. Are mobilities in hybrid organic-inorganic halide perovskites actually 'high'? *J. Phys. Chem. Lett.* **6**, 4754–4757 (2015).
- Akselrod, G. M. et al. Visualization of exciton transport in ordered and disordered molecular solids. *Nat. Commun.* **5**, 3646 (2014).

6. Penwell, S. B., Ginsberg, L. D. S., Noriega, R. & Ginsberg, N. S. Resolving ultrafast exciton migration in organic solids at the nanoscale. *Nat. Mater.* **16**, 1136–1142 (2017).
7. Kulig, M. et al. Exciton diffusion and halo effects in monolayer semiconductors. *Phys. Rev. Lett.* **120**, 207401 (2018).
8. Seo, M. A. et al. Mapping carrier diffusion in single silicon core-shell nanowires with ultrafast optical microscopy. *Nano Lett.* **12**, 6334–6338 (2012).
9. Gabriel, M. M. et al. Direct imaging of free carrier and trap carrier motion in silicon nanowires by spatially-separated femtosecond pump–probe microscopy. *Nano Lett.* **13**, 1336–1340 (2013).
10. Guo, Z., Manser, J. S., Wan, Y., Kamat, P. V. & Huang, L. Spatial and temporal imaging of long-range charge transport in perovskite thin films by ultrafast microscopy. *Nat. Commun.* **6**, 7471–7479 (2015).
11. Rozenman, G. G., Akulov, K., Golombek, A. & Schwartz, T. Long-range transport of organic exciton-polaritons revealed by ultrafast microscopy. *ACS Photon.* **5**, 105–110 (2018).
12. Najafi, E., Scarborough, T. D., Tang, J. & Zewail, A. Four-dimensional imaging of carrier interface dynamics in p–n junctions. *Science* **347**, 164–167 (2015).
13. Plakhotnik, T. & Palm, V. Interferometric signatures of single molecules. *Phys. Rev. Lett.* **87**, 183602-1–183602-4 (2001).
14. Wolpert, C. et al. Transient reflection: a versatile technique for ultrafast spectroscopy of a single quantum dot in complex environments. *Nano Lett.* **12**, 453–457 (2012).
15. Karrai, K. & Warburton, R. J. Optical transmission and reflection spectroscopy of single quantum dots. *Superlattice. Microsc.* **33**, 311–337 (2003).
16. Amos, L. A. & Amos, W. B. The bending of sliding microtubules imaged by confocal light microscopy and negative stain electron microscopy. *J. Cell Sci.* **1991**, 95–101 (1991).
17. Lindfors, K., Kalkbrenner, T., Stoller, P. & Sandoghdar, V. Detection and spectroscopy of gold nanoparticles using supercontinuum white light confocal microscopy. *Phys. Rev. Lett.* **93**, 037401 (2004).
18. Jacobsen, V., Stoller, P., Brunner, C., Vogel, V. & Sandoghdar, V. Interferometric optical detection and tracking of very small gold nanoparticles at a water-glass interface. *Opt. Express* **14**, 405–414 (2006).
19. Young, G. et al. Quantitative mass imaging of single biological macromolecules. *Science* **360**, 423–427 (2018).
20. Ortega-Arroyo, J. & Kukura, P. Interferometric scattering microscopy (iSCAT): new frontiers in ultrafast and ultrasensitive optical microscopy. *Phys. Chem. Chem. Phys.* **14**, 15625–15636 (2012).
21. Ignatovich, F. V. & Novotny, L. Real-time and background-free detection of nanoscale particles. *Phys. Rev. Lett.* **96**, 1–4 (2006).
22. Berciaud, S., Cognet, L., Blab, G. A. & Lounis, B. Photothermal heterodyne imaging of individual nonfluorescent nanoclusters and nanocrystals. *Phys. Rev. Lett.* **93**, 257402 (2004).
23. Boyer, D., Tamarat, P., Maali, A., Lounis, B. & Orrit, M. Photothermal imaging of nanometer-sized metal particles among scatterers. *Science* **297**, 1160–1163 (2002).
24. Price, M. B. et al. Hot-carrier cooling and photoinduced refractive index changes in organic–inorganic lead halide perovskites. *Nat. Commun.* **6**, 8420 (2015).
25. Yang, Y. et al. Top and bottom surfaces limit carrier lifetime in lead iodide perovskite films. *Nat. Energy* **2**, 1–7 (2017).
26. Sorenson, S. A., Patrow, J. G. & Dawlaty, J. M. Electronic dynamics in natural iron pyrite studied by broadband transient reflection spectroscopy. *J. Phys. Chem. C* **120**, 7736–7747 (2016).
27. Jacoboni, C., Canali, C., Ottaviani, G. & Quaranta, A. A review of some charge transport properties of silicon. *Solid State Phys.* **20**, 77–89 (1977).
28. Shanks, H. R., Maycock, P. D., Sidles, P. H. & Danielson, G. C. Thermal conductivity of silicon from 300 to 1400 K. *Phys. Rev.* **130**, 1743–1748 (1963).
29. Shi, D. et al. Low trap-state density and long carrier diffusion in organolead trihalide perovskite single crystals. *Science* **347**, 519–522 (2015).
30. Hill, A. H., Smyser, K. E., Kennedy, C. L., Massaro, E. S. & Grumstrup, E. M. Screened charge carrier transport in methylammonium lead iodide perovskite thin films. *J. Phys. Chem. Lett.* **8**, 948–953 (2017).
31. Anthony, J. E., Brooks, J. S., Eaton, D. L. & Parkin, S. R. Functionalized pentacene: improved electronic properties from control of solid-state order. *J. Am. Chem. Soc.* **123**, 9482–9483 (2001).
32. Giri, G. et al. Tuning charge transport in solution-sheared organic semiconductors using lattice strain. *Nature* **480**, 504–508 (2011).
33. Chen, J., Tee, C. K., Shtein, M., Anthony, J. & Martin, D. C. Grain-boundary-limited charge transport in solution-processed 6,13 bis(tri-isopropylsilyl)ethynyl pentacene thin film transistors. *J. Appl. Phys.* **103**, 114513 (2008).
34. Zhu, T., Wan, Y., Guo, Z., Johnson, J. & Huang, L. Two birds with one stone: tailoring singlet fission for both triplet yield and exciton diffusion length. *Adv. Mater.* 7539–7547 (2016). <https://doi.org/10.1002/adma.201600968>
35. Rivnay, J. et al. Large modulation of carrier transport by grain-boundary molecular packing and microstructure in organic thin films. *Nat. Mater.* **8**, 952–958 (2009).
36. Greuter, F. & Blatter, G. Electrical properties of grain boundaries in polycrystalline compound semiconductors. *Semicond. Sci. Technol.* **5**, 111–137 (1990).
37. Yun, J. S. et al. Benefit of grain boundaries in organic-inorganic halide planar perovskite solar cells. *J. Phys. Chem. Lett.* **6**, 875–880 (2015).
38. Reid, O. G., Yang, M., Kopidakis, N., Zhu, K. & Rumbles, G. Grain-size-limited mobility in methylammonium lead iodide perovskite thin films. *ACS Energy Lett.* **1**, 561–565 (2016).
39. DeQuilettes, D. W. et al. Impact of microstructure on local carrier lifetime in perovskite solar cells. *Science* **348**, 683–686 (2015).
40. DeQuilettes, D. W. et al. Tracking photoexcited carriers in hybrid perovskite semiconductors: trap-dominated spatial heterogeneity and diffusion. *ACS Nano* **11**, 11488–11496 (2017).
41. Tian, W. et al. Limiting perovskite solar cell performance by heterogeneous carrier extraction. *Angew. Chem. Int. Ed.* **55**, 13067–13071 (2016).
42. Ciesielski, R. et al. Grain boundaries act as solid walls for charge carrier diffusion in large crystal MAPI thin films. *ACS Appl. Mater. Interf.* **10**, 7974–7981 (2018).
43. MacDonald, G. A. et al. Methylammonium lead iodide grain boundaries exhibit depth-dependent electrical properties. *Energy Environ. Sci.* **9**, 3642–3649 (2016).
44. Schnedermann, C. et al. Sub-10 fs time-resolved vibronic optical microscopy. *J. Phys. Chem. Lett.* **7**, 4854–4859 (2016).
45. Snaiders, J. M. et al. Ultrafast imaging of carrier transport across grain boundaries in hybrid perovskite thin films. *ACS Energy Lett.* **3**, 1402–1408 (2018).
46. Saliba, M., Correa-Baena, J. P., Grätzel, M., Hagfeldt, A. & Abate, A. Perovskite solar cells: from the atomic level to film quality and device performance. *Angew. Chem. Int. Ed.* **57**, 2554–2569 (2018).
47. Berry, J. et al. Hybrid organic–inorganic perovskites (HOIPs): opportunities and challenges. *Adv. Mater.* **27**, 5102–5112 (2015).
48. Krishnan, M., Mojarad, N., Kukura, P. & Sandoghdar, V. Geometry-induced electrostatic trapping of nanometric objects in a fluid. *Nature* **467**, 692–695 (2010).
49. Baffou, G. et al. Thermal imaging of nanostructures by quantitative optical phase analysis. *ACS Nano* **6**, 2452–2458 (2012).
50. Celebrano, M., Kukura, P., Renn, A. & Sandoghdar, V. Single-molecule imaging by optical absorption. *Nat. Photon.* **5**, 95–98 (2011).

Acknowledgements

This work was supported by STROBE, A National Science Foundation Science and Technology Center under grant no. DMR 1548924. The manuscript revision was also supported by the Photonics at Thermodynamic Limits Energy Frontier Research Center, funded by the US Department of Energy Office of Science Basic Energy Sciences Program, under award no. DE-SC0019140. Q.Y. and H.L.W. acknowledge National Science Foundation Graduate Research Fellowship DGE 1106400. N.S.G. acknowledges an Alfred P. Sloan Research Fellowship, a David and Lucile Packard Foundation Fellowship for Science and Engineering, and a Camille and Henry Dreyfus Teacher-Scholar Award.

Author contributions

M.D. designed and built the set-up with Q.Y. M.D. and H.L.W. prepared samples and collected the data. M.D. analysed the data. N.S.G. supervised the research. M.D. and N.S.G. wrote the manuscript with input from all authors.

Competing interests

The authors declare no competing interests.

Additional information

Supplementary information is available for this paper at <https://doi.org/10.1038/s41563-019-0498-x>.

Correspondence and requests for materials should be addressed to N.S.G.

Reprints and permissions information is available at www.nature.com/reprints.

Publisher's note Springer Nature remains neutral with regard to jurisdictional claims in published maps and institutional affiliations.

© The Author(s), under exclusive licence to Springer Nature Limited 2019

Methods

Details of the experimental apparatus and sample preparation protocols are provided in the Supplementary Information.

Our implementation of stroboSCAT is illustrated in Supplementary Fig. 1. For all data shown in the text, the light sources used are two laser diodes (LDH-D-C-440 for the pump and LDH-D-C-640 for the probe, PicoQuant, with centre wavelengths of 440 and 635 nm, respectively) driven by the same laser driver. For the experiments shown in the text, we use a base laser repetition rate of 2 MHz, with the pump modulated at 660 Hz; the pump–probe delay times are controlled using the electronic delay capabilities of the driver with 20 ps resolution. The temporal pulse widths at full-width at half-maximum are ~ 100 ps.

Both the pump and the probe are spatially filtered through $20\ \mu\text{m}$ pinholes and telescoped to ~ 6 mm and 1 mm beam diameters, respectively, before entering the microscope. The two beams are combined using a longpass filter and directed to a homemade microscope of very similar design to the microscope body detailed in Ortega Arroyo et al.⁵¹ A wide-field lens with focal length $f = 300$ mm is inserted in the probe beam path upstream of the longpass filter to focus the beam in the back focal plane of the objective, resulting in wide-field illumination ($\sim 5\text{--}60\ \mu\text{m}$ depending on the beam size before the wide-field lens) of the sample. A 50/50 beam splitter reflects the pump and probe light into a high numerical aperture (1.4 NA) oil-immersion objective and onto the sample, resulting in an overlapped confocal and wide-field illumination, respectively. Probe light reflected from the sample–substrate interface as well as scattered from the sample are collected through the same objective. The light transmitted through the beam splitter is focused onto a complementary metal–oxide semiconductor detector using an $f = 500$ mm lens placed one tube-length (200 mm) away from the back focal plane of the objective. The total magnification is 157.5. The pump light is spectrally filtered out in the stroboSCAT configuration. For wide-field emission, other appropriate emission filter arrangements are used for any given sample. Optional

half- or quarter-waveplates are used to control the polarization of pump and probe beams in polarization-sensitive measurements, such as for TIPS-Pn.

For spectral interferometry measurements, the same event sequence, camera model and pump pulse excitation are used, but instead of using a narrowband probe, we use a broadband white light probe. The white light probe is generated by focusing the fundamental output (1,030 nm, 200 kHz) of a Light Conversion PHAROS ultrafast regeneratively amplified laser system into a 3 mm yttrium–aluminium garnet crystal. For the spectral interferometry data on MAPbI₃, the white light output is filtered with a 675 nm longpass filter to reduce sample exposure to above-bandgap light. The white light is sent collimated into the objective to obtain near-diffraction-limited probe pulses. The reflected light is then coupled into a home-built prism spectrometer and dispersed onto a complementary metal–oxide semiconductor camera. The entrance slit of the spectrometer is placed in the image plane. The electronic delays between pump and probe are controlled using an external delay generator, triggered with the pulse output of the ultrafast laser and feeding a user-delayed signal to the diode driver.

The use of electronic delays and modulation as well as a wide-field probe results in no moving parts in the set-up (apart from optional shutters), leading to an extremely stable and compact ($<1\ \text{m}^2$) set-up.

Data availability

All raw data are displayed in Figs. 1–3 of the main text and Supplementary Figs. 2–24. Raw image files are available on reasonable request from the corresponding author.

References

- Ortega Arroyo, J., Cole, D. & Kukura, P. Interferometric scattering microscopy and its combination with single-molecule fluorescence imaging. *Nat. Protoc.* **11**, 617–633 (2016).